Tunable nonlinear anisotropic Rashba splitting in monolayer transition metal dichalcogenide $MoS_{2(1-x)}Se_{2x}$ alloys

Souvick Chakraborty [1,*] and Satyabrata Raj [1,2]

[1]*Department of Physical Sciences, Indian Institute of Science Education and Research Kolkata, Mohanpur, Nadia, West Bengal 741246, India*

[2]*National Centre for High-Pressure Studies, Indian Institute of Science Education and Research Kolkata, Mohanpur, Nadia, West Bengal 741246, India*

(Received 25 May 2023; revised 17 September 2023; accepted 20 September 2023; published 2 October 2023)

We investigate the Rashba effect in thermodynamically stable nonpolar transition metal dichalcogenide (TMD) alloys of the form $MoS_{2(1-x)}Se_{2x}$ in the presence of an out-of-plane electric field using first-principles calculations. These alloys exhibit a nonlinear anisotropic Rashba effect, which is explained by considering symmetry-dependent higher-order terms in the Rashba Hamiltonian. Of the three stable alloys studied here, $MoS_{0.67}Se_{1.33}$ and $MoS_{1.33}Se_{0.67}$ belong to the same symmetry group as MoS_2 and $MoSe_2$, and the anisotropy in their Rashba splitting originates mainly from a single anisotropic third-order term in the Hamiltonian. On the other hand, the MoSSe alloy belongs to the C_{2v} point group symmetry, where all the first- and third-order parameters are anisotropic and significantly contribute to the anisotropy of the Rashba effect. Furthermore, the Rashba energy splitting in these nonpolar alloys can be extensively tuned and enhanced significantly by applying a perpendicular external electric field and biaxial strain, making them promising candidates for spintronic applications.

DOI: 10.1103/PhysRevB.108.165402

I. INTRODUCTION

Over the last few decades, monolayer transition metal dichalcogenides (TMDs) have gained prominence in the field of nano-optics and nanoelectronics due to their direct band gaps lying mostly in the visible range [1–3], high electron mobility [4,5], high on-off current ratio [4,6], and large exciton binding energy [7,8]. This family of materials has emerged as the frontrunner to replace silicon in modern transistors to meet the constant need for downsizing electronic devices [9,10]. Their exceptional mechanical strength and layer-dependent band gaps also make them ideal candidates for constructing flexible and tunable electronic devices [11–13]. TMDs exist in the chemical form MX_2, where the transition metal M is sandwiched between two identical layers of chalcogen X atoms. The most popular of these materials are the group-6 monolayer TMDs, notably those with M = Mo, W, and X = S, Se, which have a trigonal prismatic (1H) coordination for the metal atom and a hexagonal crystal structure identical to graphene. However, unlike graphene, the space inversion symmetry is broken in these materials due to the presence of two different atoms in the basis. The broken in-plane inversion symmetry and the large spin-orbit splitting from the metal d orbitals give rise to coupling between the valley and the spin degrees of freedom, which can then be used to store information using optical excitations of different helicities [14–17]. Although the in-plane inversion asymmetry endows these materials with certain benefits over graphene, the out-of-plane mirror symmetry breaking can introduce even more remarkable features.

Researchers have recently shown that breaking the mirror symmetry in these materials can result in a physical phenomenon called the Rashba effect [18]. An intrinsic out-of-plane potential gradient can introduce mirror asymmetry in these systems, resulting in the momentum-dependent Rashba splitting of the bands. A special type of TMD materials with broken mirror symmetry called Janus TMDs was theoretically proposed by Cheng *et al.* [19]. The Janus TMDs, with the chemical formula MXY, consist of two distinct chalcogen atom (X and Y) layers sandwiching the single metal atom (M) layer, producing an intrinsic electric field in the out-of-plane direction. The Janus MoSSe structure was realized experimentally by selenizing one of the S layers in the monolayer of MoS_2 [20]. The uniform distribution of the electric dipoles in this system gives rise to an isotropic Rashba effect, which has proved critical for realizing spin-charge interconversion [21–23]. However, their low thermodynamic stability and difficulty of synthesis have led to the search for more stable alternate materials with similar or better functionalities.

Another way to introduce the Rashba effect in nonpolar TMDs is by applying an external electric field in the out-of-plane direction [24,25]. In the presence of a small electric field, conventional TMDs exhibit a uniform linear Rashba effect identical to the Janus alloys. However, the effect becomes nonlinear at higher electric fields and increases up to an order of magnitude higher than the Janus structures and comparable with that in heavy metal surfaces [26]. For the linear Rashba effect, a simple Bychkov-Rashba Hamiltonian [18,27,28] of

*sc20rs042@iiserkol.ac.in

 ©2023 American Physical Society

the form:

$$H_R(\vec{k}) = \alpha_R(k_x\sigma_y - k_y\sigma_x), \quad (1)$$

is sufficient to describe the k-dependent splitting occurring in the polar Janus structures. Here, α_R is known as the Rashba parameter, and $\vec{k}$ and $\vec{\sigma}$ denote the electron momentum and Pauli matrices, respectively. The linear isotropic Rashba effect observed in the polar Janus structures does not offer much tunability, and even under the influence of an external electric field, the enhancement of the Rashba parameter is insignificant compared with the unmodified TMD materials [26]. On the other hand, introducing anisotropy to the Rashba effect can induce intrinsic tunability to the system and lead to a direction-dependent Rashba Edelstein effect [29]. The symmetry of the system plays a crucial role in dictating the anisotropy present in the Rashba effect [30,31]. For example, the Rashba effect observed in systems with C_{2v} symmetry is usually anisotropic with anisotropic effective masses and is characterized by two independent Rashba parameters instead of one [32–34]. The nonlinearity and anisotropy observed in TMDs at high electric fields, on the other hand, cannot be explained by the linear Rashba Hamiltonian unless a more complex symmetry-dependent Hamiltonian containing higher order k terms is considered. Unfortunately, all the popular group-6 TMDs share identical point group symmetry and electronic properties, which prevents us from observing the role of symmetry and atomic composition on the nature of the Rashba effect. Alloying can be an effective way to generate structures with different compositions and symmetries without removing the beneficial aspects of the parent compounds.

Researchers have been exploring TMD alloys beyond the Janus ones to find two-dimensional materials with adjustable electronic properties. In contrast to their binary compounds, which have a fixed band gap value, these alloys come with a wide range of band gaps and electronic properties [35–40] and are often more stable than the Janus TMDs. As such, authors of multiple experimental studies have reported their controlled synthesis [37–41]. Moreover, they can also exhibit some intriguing physics owing to their unique atomic configurations and symmetries [32]. The band gap E_g of a monolayer TMD alloy with the formula $MY_{2(1-x)}Z_{2x}$ can be tuned as a function of its alloy composition according to the formula:

$$E_g(x) = (1-x)E_g(0) + xE_g(1) - \Omega x(1-x), \quad (2)$$

where Ω depicts the bowing parameter. Depending upon the atomic arrangement, alloys with the same chemical formula can be classified into different configurations with varying ground state (GS) energies. The thermodynamic stability of a particular configuration φ can be characterized by its formation energy which, for an alloy with the formula $MY_{2(1-x)}Z_{2x}$, is expressed as

$$E_f(\varphi) = E_{MY_{2(1-x)}Z_{2x}}(\varphi) - (1-x)E_{MY_2} - xE_{MZ_2}, \quad (3)$$

where E_{MY_2} and E_{MZ_2} denote the GS energies of the two parent compounds. Identifying the most stable GS for the different alloy compositions using only density functional theory (DFT) can be quite challenging, as it requires investigating all possible configurations. In this regard, the cluster expansion (CE) method has successfully simplified the problem and has been applied to various alloy systems [36,42,43].

In this paper, we study the role of symmetry on the nature of the electric-field-induced Rashba effect observed in different nonpolar TMD alloys of the form $MoS_{2(1-x)}Se_{2x}$ under different conditions of biaxial strain and external electric field. We started by calculating the GS configurations for the alloys using the CE method in conjunction with DFT and obtained GSs with different symmetries for $x = 0.33$, 0.5, and 0.67. Our DFT studies indicate that these alloys exhibit nonlinear and anisotropic Rashba effect in the presence of a vertical electric field, whose origin is dependent on the crystal symmetry. Out of the three alloys, $MoS_{0.67}Se_{1.33}$ and $MoS_{1.33}Se_{0.67}$ belong to the D_3 point group, where the anisotropy arises from a single anisotropic third-order term in the Rashba Hamiltonian, exactly like the group-6 TMD monolayers, whereas in case of the non-Janus MoSSe alloy, the C_{2v} point group ensures that the anisotropic contribution comes from both the first- and third-order parameters of the Hamiltonian. The magnitude and anisotropy of this Rashba effect depend on the relative chalcogen composition ratio (x) and can be significantly enhanced by increasing the external electric field or applying compressive biaxial strain. Our results regarding the strain and electric field tunable anisotropic Rashba effect in these TMD alloys can be measured experimentally using spin-resolved angle-resolved photoemission spectroscopy [44,45] and open possibilities for designing optoelectronic and spintronic devices.

II. COMPUTATIONAL DETAILS

All first-principles DFT calculations in this paper are performed with VASP software [46] using the generalized gradient approximation exchange-correlation functional in the form of Perdew-Burke-Ernzerhof [47]. All the calculations employ the frozen-core projector augmented-wave [48] technique to reduce the computational cost and a sufficiently high energy cutoff of 600 eV for the plane-wave basis. A vacuum space of at least 18 Å is implemented along the z axis to prevent any interlayer interactions with the periodic images.

The CE method, in conjunction with the DFT calculations, is used to calculate the convex hull diagram for the $MoS_{2(1-x)}Se_{2x}$ alloys. For this purpose, the formation energies of $\sim$87 alloy structures with up to 24 atoms per unit cell are evaluated using DFT calculations. These are then used to generate the CE with the help of the ATAT code [49] and predict the formation energies of a further $\sim$8000 structures. The cross-validation score is found to be $\sim$0.46 meV, which indicates an exceptionally good CE fit.

A dynamic k-point grid is adopted for the structural optimization of the alloys in such a way that the product of the number of atoms and the k points is $\sim$1200, with the number of k points along the c axis kept fixed at 1. For the self-consistent field calculations, a higher-density k-point grid was chosen based on the size of the supercell. The Hellmann-Feynman force tolerance for the optimization step was set to a value of 5 meV/Å, whereas the total energy convergence criteria for the self-consistent loop are kept at 10^{-8} eV. The band structure calculations are performed along the $\Gamma-M-K-\Gamma$ path. The phonon band structures are calculated with the help

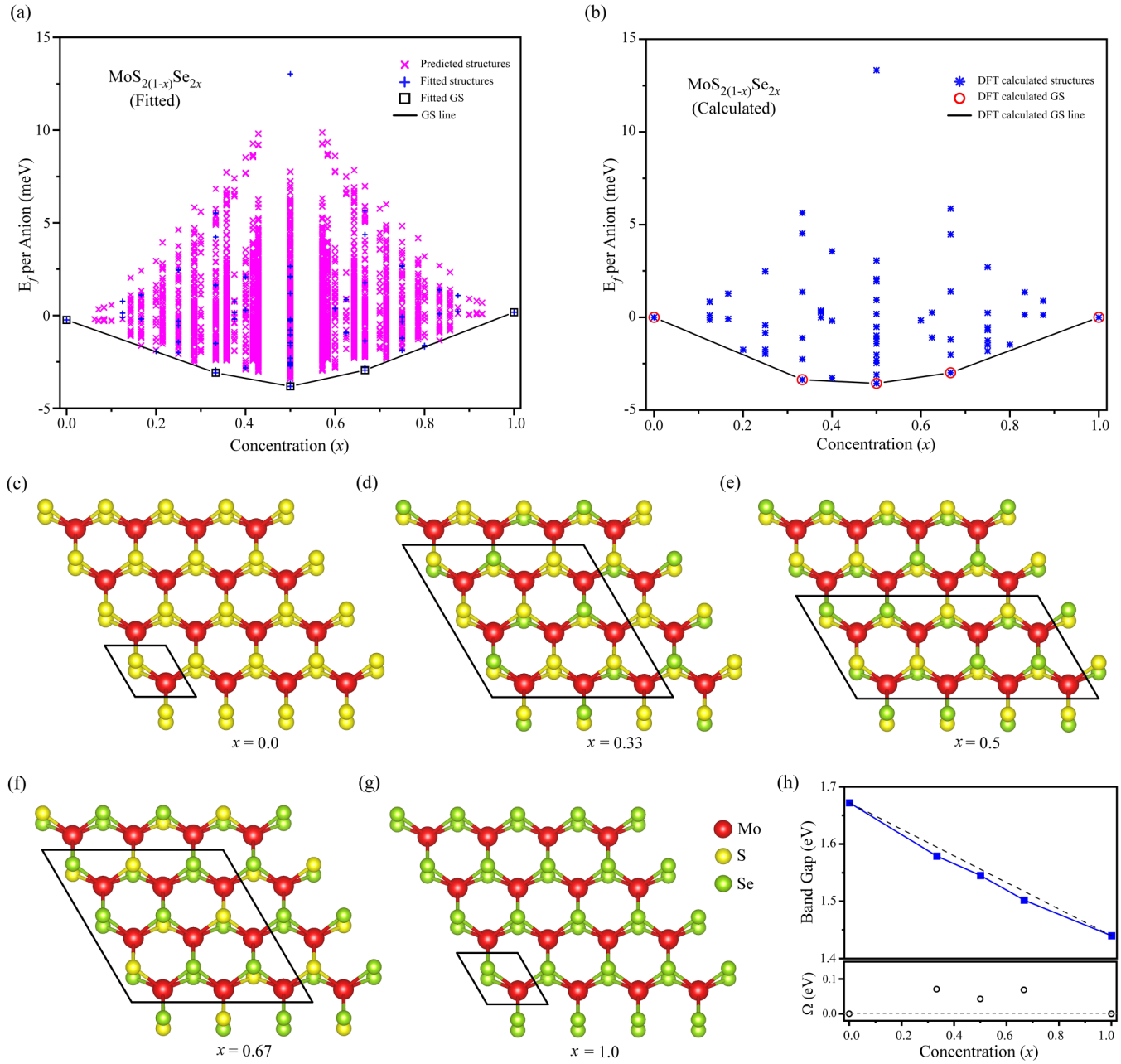

FIG. 1. Formation energies (E_f) and the ground state (GS) lines of the $MoS_{2(1-x)}Se_{2x}$ alloys obtained from (a) cluster expansion fit and (b) DFT-PBE calculation results. (c)–(g) Thermodynamically stable GS monolayer structures of (a) MoS_2, (b) $MoS_{1.33}Se_{0.67}$, (c) MoSSe, (d) $MoS_{0.67}Se_{1.33}$, and (e) $MoSe_2$. (h) Band gap and bowing parameter (Ω) of the band gap vs alloy composition (x).

of the PHONOPY package [50] to evaluate the dynamic stabilities, and the spin texture near the Γ point is plotted using the PYPROCAR code [51].

III. RESULTS AND DISCUSSIONS

The formation energies (E_f) of all the $MoS_{2(1-x)}Se_{2x}$ alloys obtained from the CE simulation results are provided in Fig. 1, with the CE fitted results shown in Fig. 1(a) and the DFT calculated ones shown in Fig. 1(b). We obtain three thermodynamically stable GS structures at three different compositions for $x = 0.33$, 0.5, and 0.67, which are shown in Figs. 1(d)–1(f). These structures are found to be the same as in previous works [36], although we have used a higher energy cutoff and lower tolerance values for force and energy convergence in our DFT calculations. Our phonon band structure calculations show all three structures to be dynamically stable (see Fig. S2 in the Supplemental Material [52]) and thus pave the path for their experimental synthesis, providing TMD alloys with different electronic properties. Incidentally, these $MoS_{2(1-x)}Se_{2x}$ alloy GS configurations are like those obtained from the CE simulations of $WS_{2(1-x)}Se_{2x}$ (with the Mo atoms replaced by W), which are also thermodynamically stable [36], indicating that our analyses should be valid for W-based alloys as well. The other ordered ternary alloy configurations involving tellurium [(S, Te) and (Se, Te)] are all

found to have positive formation energies in the CE, and as such, no GSs can be determined for them [36]. From our CE results, it is observed that the aggregation of S or Se atoms is discouraged in structures with negative formation enthalpies, and the alloys with the maximum separation between two neighboring chalcogen atoms of the same species are usually the most stable. For example, the Janus structure, in which each mirror site of a particular chalcogen atom is occupied by a chalcogen of a different species, has a positive formation energy of $\sim+13.5$ meV/anion and an average S-S distance of 3.2495 Å, considering its six nearest neighbors. The most stable MoSSe structure ($E_f = -3.6$ meV/anion), on the other hand, not only has different chalcogen atoms in the mirror sites but also at the nearest in-plane neighboring site with an average S-S distance of 4.0366 Å for the nearest six neighbors (see Fig. S3 in the Supplemental Material [52]). This tendency of developing distinct chalcogen atom pairs leads to a beneficial charge distribution over the metal-chalcogen bonds, stabilizing the alloy structure [32].

Both the CE-fitted and the DFT-calculated convex hulls are constructed using the primitive unit cells for all the alloys. Once the GSs are calculated, we switch to the hexagonal unit cells [shown in Figs. 1(c)–1(g)] to properly compare their electronic properties with the conventional TMDs. The calculated formation energies of the three alloy structures for $x = 0.33,\ 0.5,$ and 0.67 are ~-3.4, -3.6, and -3.0 meV per anion, respectively, and are independent of the choice of the unit cell. Thus, the MoSSe alloy can be considered the most thermodynamically stable alloy, closely followed by $MoS_{1.33}Se_{0.67}$ and $MoS_{0.67}Se_{1.33}$. The CE-fitted results show the same trend. The $MoS_{1.33}Se_{0.67}$ and $MoS_{0.67}Se_{1.33}$ structures are geometrically identical, where one can be obtained by interchanging the S and Se atoms of the other, followed by a structural optimization. These two structures, with 27 atoms each, have hexagonal symmetries with lattice constants of 9.809 and 9.672 Å, respectively. The MoSSe structure, on the other hand, slightly deviates from the hexagonal symmetry, where one of the in-plane lattice constants differs by $\sim$0.05% from the other. This type of in-plane asymmetry can often result in unusual physical phenomena [32]. Although alloys with different compositions have completely different lattice constants, the Mo-S and Mo-Se bond lengths remain more or less consistent in these structures and match those of pure MoS_2 and $MoSe_2$. The reason behind the preservation of the metal-chalcogen bond lengths in these alloys has been explained well by Kang *et al.* [36].

Monolayer MoS_2 and $MoSe_2$ are both direct band gap (unlike its bulk form, which has indirect band gap) semiconductors with the band extrema lying at the K point. The operating band gaps of semiconductors usually vary for different applications, and monolayer MoS_2 and $MoSe_2$ have been experimentally shown to have ideal band gaps for photoelectrochemical water splitting [53] and solar energy conversion [54], respectively. Our nonrelativistic DFT simulations show that the $MoS_{2(1-x)}Se_{2x}$ alloys possess similar band features with direct band gaps of different magnitudes, making them suitable for a wide variety of applications. The band gaps for the $MoS_{2(1-x)}Se_{2x}$ family decrease with an increase in the alloy composition (x) from 1.67 eV for MoS_2 ($x = 0$) to 1.44 eV for $MoSe_2$ ($x = 1$), and the variation is plotted in Fig. 1(h) along with the bowing parameter (Ω). The magnitude of the band gap as well as the location of the band extrema can prove decisive while designing spin-charge interconversion devices based on the Rashba effect. Thus, before calculating the Rashba effect, it is important to study the effect of biaxial strain and external electric field on the overall band structure. The band structures of pure TMDs exhibit high sensitivity to mechanical strain, which has made strain engineering a viable technique for tuning their band gaps [55–58]. Authors of previous studies have shown that the effect of strain depends on the nature of the chalcogen atoms present in the TMDs [57,59]. In this paper, we have performed a comparative analysis of the band structures of MoS_2, $MoSe_2$, and the three alloys under biaxial strain, and the results are presented in Fig. 2(a). To preserve the symmetry of the systems, we have applied an equal amount of strain along the two in-plane lattice directions and have quantized it by $\varepsilon = (a - a_0)/a_0$ in percentage. Here, a is the lattice constant of the strained lattice, and a_0 is that of the unstrained structure. The applied biaxial strain ranges from -5 to $+5$% for all structures, where the negative and positive values correspond to compressive and tensile strain, respectively. It is observed that the compressive strain enhances the equilibrium band gap, whereas the tensile strain reduces it for all the structures. However, in both cases, the band gaps shift from direct to indirect after a relatively small amount of strain. The change in the band gap type for the MoSSe alloy has been shown in the inset of Fig. 2(a) as an example. With an increase in the compressive strain, the band gap first rises until ~-2% strain and then gradually starts to decrease for all alloys. At -3% strain, MoS_2 attains its maximum band gap of $\sim$1.91 eV, which is also the highest among all the structures. The other alloys reach their maximum at ~-2% compressive strain, with lower band gaps for structures with higher Se content. The band gaps of $MoSe_2$, $MoS_{0.67}Se_{1.33}$, MoSSe, and $MoS_{1.33}Se_{0.67}$ at -2% strain are 1.59, 1.64, 1.73, and 1.75 eV, respectively. With an increase in the tensile strain, all the band gaps monotonically decrease up to the last collected data point at 5%, where they attain their minima. Authors of previous studies have reported that the application of either very high compressive or tensile strain causes a semiconductor-to-metallic transition in MoS_2 and $MoSe_2$ [55,58]. In this paper, we observed that the tensile strain aided semiconductor-to-metal transition of the alloys occurs in the range of 16–19% strain. However, such high strain can cause major changes in the crystal structure and is best suited to study experimentally.

In Fig. 2(b), we have plotted the band structures of MoS_2 and $MoSe_2$ at -5, 0, and $+5$% strain. To effectively compare the band structures, we have scaled the strained structures so that the high-symmetry points overlap with those of the unstrained ones. For both structures, the direct band gaps at relatively low strain occur at the K point. On the other hand, the indirect band gap appears between the valence band maximum (VBM) at the K point and the conduction band minimum (CBM) at the λ point at higher compressive strain and between the Γ (VBM) and K (CBM) points at high tensile strain. Although both TMDs show a similar band gap vs strain profile, there are some subtle differences in their band structures, primarily in the valence bands. For MoS_2, the bands near the Γ point for 5 and 0% strain almost overlap, whereas

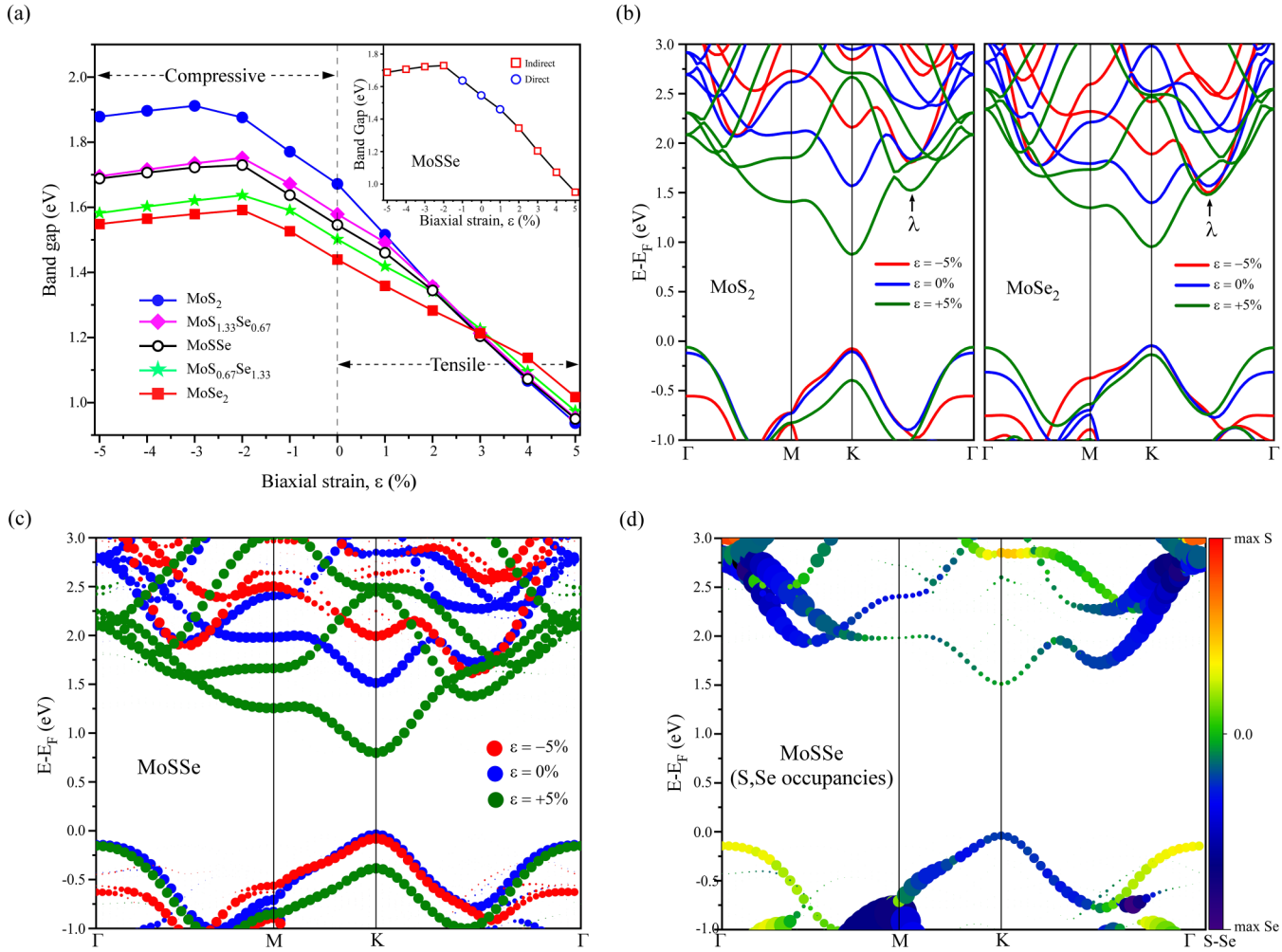

FIG. 2. (a) Band gap variation of all $MoS_{2(1-x)}Se_{2x}$ alloys as a function of the applied biaxial strain (ε). The change of direct to indirect gap of MoSSe with the applied strain is shown in the inset. (b) Band structures of MoS_2 and $MoSe_2$ at −5% (red), 0% (blue), and 5% (olive) strain. (c) Unfolded band structures of MoSSe at −5% (red), 0% (blue), and 5% (olive) strain. (d) Unfolded band structure of MoSSe with the differential occupancies of the S and Se atoms. The point size represents the overall contribution of the chalcogen atoms, while the color represents the dominant species.

those in $MoSe_2$ are well separated in energy. Similarly, there is an overlap of the valence bands at −5 and 0% strain near the *M* point in MoS_2, which is not the case for $MoSe_2$. To identify which of the two chalcogens plays a dominating role in the alloy band structures, we have plotted the unfolded band structures of the MoSSe alloy at the three different strain values in Fig. 2(c). It can be seen that the valence bands near the Γ point are like those in MoS_2, whereas those near the *M* point show identical behavior to the bands in $MoSe_2$. To determine the contribution of the two chalcogen species in the MoSSe band structure at 0% strain, we have plotted the differential occupancies of the S and Se atoms in Fig. 2(d). The size of the points denotes the total contribution of the chalcogen atoms, and the color denotes the prevalent species. It appears that the final valence band near the Γ point has the majority of the contribution from the S atoms, which can explain its similarity with the MoS_2 structure around the Γ point. In contrast, the valence band near the *M* point has predominantly Se character, causing them to behave like $MoSe_2$. Similar atomic contributions are maintained at +5 and −5% strain too, which explains the behavior of the alloy band structures under strain. The folded band structures of $MoS_{0.67}Se_{1.33}$ and $MoS_{1.33}Se_{0.67}$ at the three strain values and their relative chalcogen occupancies at equilibrium are plotted in Fig. S4 in the Supplemental Material [52]. As expected, the $MoS_{0.67}Se_{1.33}$ and the $MoS_{1.33}Se_{0.67}$ structures have predominant Se and S characters in their valence and conduction bands, providing them with $MoSe_2$- and MoS_2-like behavior, respectively. However, there is an exception at the *M* point, which always has a Se-rich character.

The application of an external electric field can also cause noticeable changes in the band structures of the binary parent TMD materials [56]. Here, we have studied the behavior of all the stable alloys in the presence of an electric field applied perpendicularly, and the results are presented in Fig. 3(a). The variation of the band gap type for the MoS_2, MoSSe, and $MoSe_2$ structures is shown in Fig. S5 in the Supplemental Material [52]. For all the structures, we observe direct-to-indirect as well as semiconductor-to-metallic transitions as we increase the electric field. The band gap variation is found

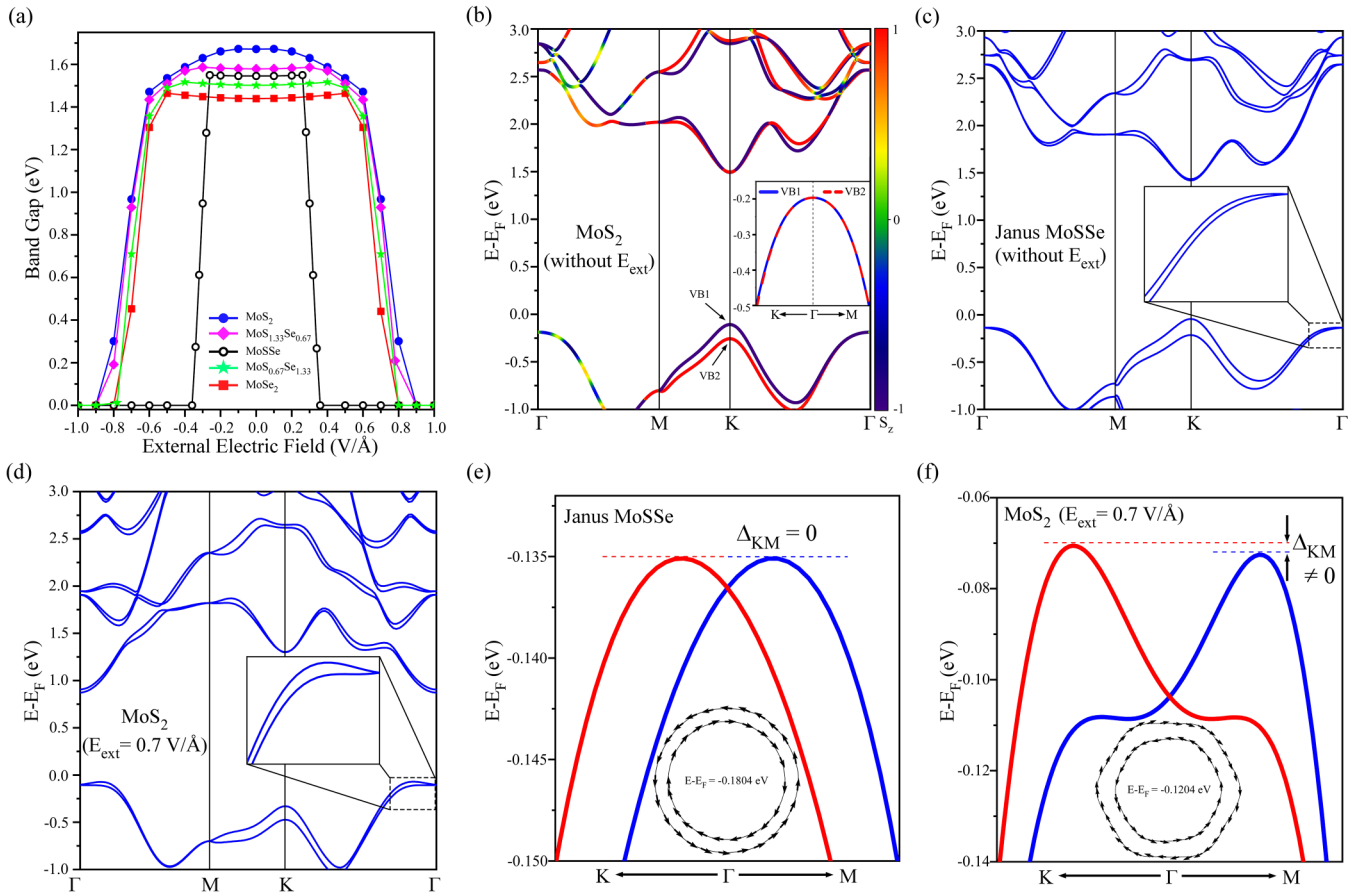

FIG. 3. (a) Electric field dependence of the band gap of $MoS_{2(1-x)}Se_{2x}$ alloys. (b) Relativistic band structure of nonpolar MoS_2 with spin projection of S_z operator. The absence of any spin splitting is shown in the inset. (c) Band structure of the polar Janus MoSSe showing the Rashba effect. (d) Band structure of monolayer MoS_2 under a perpendicular external electric field of 0.7 V/Å with Rashba splitting at the Γ point. Zoomed-in band structures and spin textures near the Γ point of (e) Janus MoSSe and (f) monolayer MoS_2 under an electric field. While the Janus MoSSe displays isotropic and linear Rashba effect, MoS_2 displays anisotropic and nonlinear Rashba effect.

to be more or less symmetric with respect to the direction of the applied electric field, which is obvious for nonpolar materials. Except for MoSSe, the band gaps of all the alloys remain indifferent until ∼0.5 to 0.6 V/Å and undergo semiconductor-to-metallic transition at ∼0.8 to 0.9 V/Å. This insensitivity of the band gaps in monolayer MoS_2 and $MoSe_2$ to relatively low electric fields has led researchers to explore the sensitive indirect band gaps in bilayer TMD systems [60–62]. Our results show that the MoSSe alloy shows a semiconductor-to-metallic transition at a very low electric field of ∼0.35 V/Å, unlike other monolayer TMD alloys (for $x = 0.0,\ 0.33,\ 0.67,$ and 1.0), making it valuable for tunable optoelectronic applications. We have further calculated the band gap variation of some trivial MoSSe alloys with different symmetries and atomic arrangements in the presence of an electric field (see Supplemental Material [52]), and the results indicate that the unique behavior of the stable alloy in this paper stems from both its chemical compositions and unique arrangement of the chalcogen atoms. Moreover, for all the alloys, the valence band extremum of the indirect band gaps shifts very close to the Γ point where the Rashba splitting occurs, providing easy access to efficiently utilize the Rashba effect.

So far, our study has been conducted without considering any relativistic effects, which has prevented us from observing any spin-orbit coupling (SOC) effects present in the systems. Our primary aim in applying an electric field is to study the feasibility of introducing the Rashba effect in these nonpolar alloys, which requires the SOC effect to be considered. To demonstrate the role of SOC in TMDs, we first calculated the relativistic band structure of monolayer MoS_2 along with the S_z spin projection, as shown in Fig. 3(b). The large Zeeman-like spin-orbital splitting observed at the high-symmetry K points in these TMD materials is attributed to the combination of the quasi-two-dimensional electronic motion and the in-plane potential gradient asymmetry, giving rise to out-of-plane spin polarizations [63]. Conversely, the Γ point does not show any type of spin splitting [see inset of Fig. 3(b)]. Polar TMDs, like the Janus structure, show not only a Zeeman-type splitting at the K point but also an in-plane Rashba-like spin splitting at the Γ point [see inset of Fig. 3(c)], providing them an advantage over the traditional TMDs. The Rashba effect is introduced in the nonpolar TMD monolayer alloys by applying an out-of-plane electric field. The band structure of monolayer MoS_2 at an external field of 0.7 V/Å is shown in Fig. 3(d). The band structure exhibits significant

spin splitting at both the K and Γ [see inset of Fig. 3(d)] points. To compare the Rashba effect in MoS_2 in the presence of an external electric field and the polar Janus MoSSe structures, we have calculated the band structures and the spin textures near the Γ point for both the structures, and the results are plotted in Figs. 3(e) and 3(f), respectively. The signatures of the Rashba splittings are entirely different, with the splitting in the Janus structure being linear and uniform, whereas that in the MoS_2 displays nonlinearity and anisotropy. The Fermi spin texture near the Γ point for the Janus structure consists of two concentric circles with opposite spin orientations typical of the conventional isotropic Rashba effect. The MoS_2 structure, on the other hand, contains two concentric hexagonal Fermi contours revealing the anisotropy in the k space. The extent of anisotropy in the Rashba splittings has been quantified in terms of the anisotropic energy (Δ_{KM}), which is defined as the energy difference between the valence band maxima along the Γ-M and Γ-K directions. Here, Δ_{KM} has a nonzero value for the MoS_2 structure, unlike Janus MoSSe, which has zero anisotropic splitting.

Unlike the linear isotropic Rashba effect in the Janus TMDs, the nonlinear Rashba splitting is extremely sensitive to the applied external field and cannot be explained simply by the two-dimensional electron gas Rashba Hamiltonian. All the monolayer group-6 binary TMDs, including MoS_2 and $MoSe_2$, have D_{3h} point group symmetry, which breaks down under the presence of an out-of-plane electric field into the C_{3v} point group. Using the $\mathbf{k}\cdot\mathbf{p}$ perturbation theory, the Hamiltonian of a C_{3v} system with up to third-order terms in k can be written as [31]

$$H_R(\vec{k}) = \left(\alpha_1 k + \alpha_3^1\, k^3\right)(\cos\theta\sigma_y - \sin\theta\sigma_x) + \alpha_3^2\, k^3 \cos 3\theta\sigma_z. \tag{4}$$

In this paper, we have defined the k_x axis along the Γ-K direction and θ as the angle between the $\vec{k}$ vector and the k_x axis. The third-order Rashba parameters can be loosely defined from the $\mathbf{k}\cdot\mathbf{p}$ perturbation theory as

$$\alpha_3^1 = \frac{\hbar^4}{4m^4\, c^2} \sum_{n,m} \frac{\langle\Phi_0|p_x|\Phi_n^+\rangle\langle\Phi_n^+|\partial_z V|\Phi_m^+\rangle\langle\Phi_m^+|p_x|\Phi_0\rangle}{\left(\epsilon_0 - \epsilon_n^E\right)\left(\epsilon_0 - \epsilon_m^E\right)}, \tag{5}$$

and

$$\alpha_3^2 = \frac{\hbar^4}{4m^4\, c^2} \sum_{n,m} \frac{\langle\Phi_0|p_x|\Phi_n^+\rangle\langle\Phi_n^+|\partial_x V|\Phi_m^-\rangle\langle\Phi_m^-|p_x|\Phi_0\rangle}{\left(\epsilon_0 - \epsilon_n^E\right)\left(\epsilon_0 - \epsilon_m^E\right)}, \tag{6}$$

where V is the crystal potential and Φ the Bloch function corresponding to the Bloch states of the system [31]. It is evident that both the first-order term α_1 and the first third-order term α_3^1 are proportional to the out-of-plane potential gradient, whereas the second third-order term α_3^2 is dependent on the in-plane potential gradient $\partial_x V$. The square of the energy difference between the two eigenvalues of the Hamiltonian in Eq. (4) is given as

$$[\Delta E(k,\theta)]^2 = \left(\alpha_1 k + \alpha_3^1\, k^3\right)^2 + \left(\alpha_3^2\right)^2 k^6 \cos^2 3\theta, \tag{7}$$

where $\Delta E(k) = [\epsilon_+(k) - \epsilon_-(k)]/2$. The first third-order term is isotropic and adds nonlinearity to the Rashba effect at high electric fields, whereas the second one adds anisotropy in the Brillouin zone due to the presence of the $\cos 3\theta$ term with it. The Rashba split bands of a C_{3v} symmetric structure obtained from the DFT calculations can be readily fitted to Eq. (7) to obtain the three parameters. Like MoS_2 and $MoSe_2$, $MoS_{1.33}Se_{0.67}$ and $MoS_{0.67}Se_{1.33}$ are perfectly hexagonal structures with D_3 point group symmetry, which is isomorphic to the C_{3v} group, and follow Eq. (4). As an example, the squared Rashba energy splitting of $MoS_{0.67}Se_{1.33}$ at an electric field of 0.6 V/Å is shown in Fig. 4(a). Typically, the linearity in $[\Delta E(k)]^2$ lasts up to 0.06–0.08 $Å^{-1}$, and using a parabolic fit (shown in olive green color) within that range, we end up with a value of $\sim$0.236 eVÅ for the first-order Rashba term α_1, which is significantly higher than MoS_2 but less than $MoSe_2$. As we have considered the Γ-K direction as the k_x axis, we can obtain the value of α_3^1 by fitting the equation:

$$[\Delta E(k, \theta = \pi/2)]^2 = \left(\alpha_1 k + \alpha_3^1\, k^3\right)^2, \tag{8}$$

along the Γ-M ($\theta = \pi/2$) direction and using the value of α_1. Similarly, the anisotropic term α_3^2 can be derived by fitting the band splitting along the Γ-K direction with Eq. (7) and putting $\cos^2 3\theta = 1$ once α_1 and α_3^1 are known. The values of α_3^1 and α_3^2 come out to be -0.915 and $1.128\,\text{eVÅ}^3$, respectively, which are also intermediate to MoS_2 and $MoSe_2$. The squared Rashba splitting energy for MoS_2, $MoS_{1.33}Se_{0.67}$, and $MoSe_2$ along the Γ-M and Γ-K directions after fitting are presented in Fig. S7 in the Supplemental Material [52].

The effect of the external electric field is completely different on the MoSSe structure due to its distinct symmetry. The MoSSe alloy has a slightly broken hexagonal symmetry and belongs to the C_{2v} point group. It is already known that the C_{2v} structure has two independent anisotropic first-order Rashba parameters along the two reciprocal axes. However, things get interesting once the higher-order terms are considered. For the C_{2v} symmetry, we end up with four third-order terms instead of two [31]. We can assign two first-order Rashba parameters $\alpha_{R,x}$ and $\alpha_{R,y}$ for the linear terms and four third-order parameters α_3^1, α_3^2, α_3^3, and α_3^4 corresponding to the four different third-order Rashba terms (see Table S1 in the Supplemental Material [52]). The Hamiltonian can then be written as

$$H_R(\vec{k}) = A(\theta)\cos\theta\sigma_y - B(\theta)\sin\theta\sigma_x, \tag{9}$$

with

$$A(\theta) = \alpha_{R,x}k + \left(\alpha_3^1\cos^2\theta + \alpha_3^3\sin^2\theta\right)k^3, \tag{10}$$

$$B(\theta) = -\alpha_{R,y}k - \left(\alpha_3^2\cos^2\theta + \alpha_3^4\sin^2\theta\right)k^3. \tag{11}$$

The absence of any σ_z term in the above Rashba Hamiltonian means that, unlike the C_{3v} Hamiltonian, the $\cos 3\theta$ term cannot be singled out for the anisotropic contribution. Instead, in this case, both $A(\theta)$ and $B(\theta)$ contribute to the nonlinearity and anisotropy of the Rashba effect. Furthermore, the squared energy splitting is given as

$$[\Delta E(k,\theta)]^2 = [A(\theta)]^2\cos^2\theta + [B(\theta)]^2\sin^2\theta. \tag{12}$$

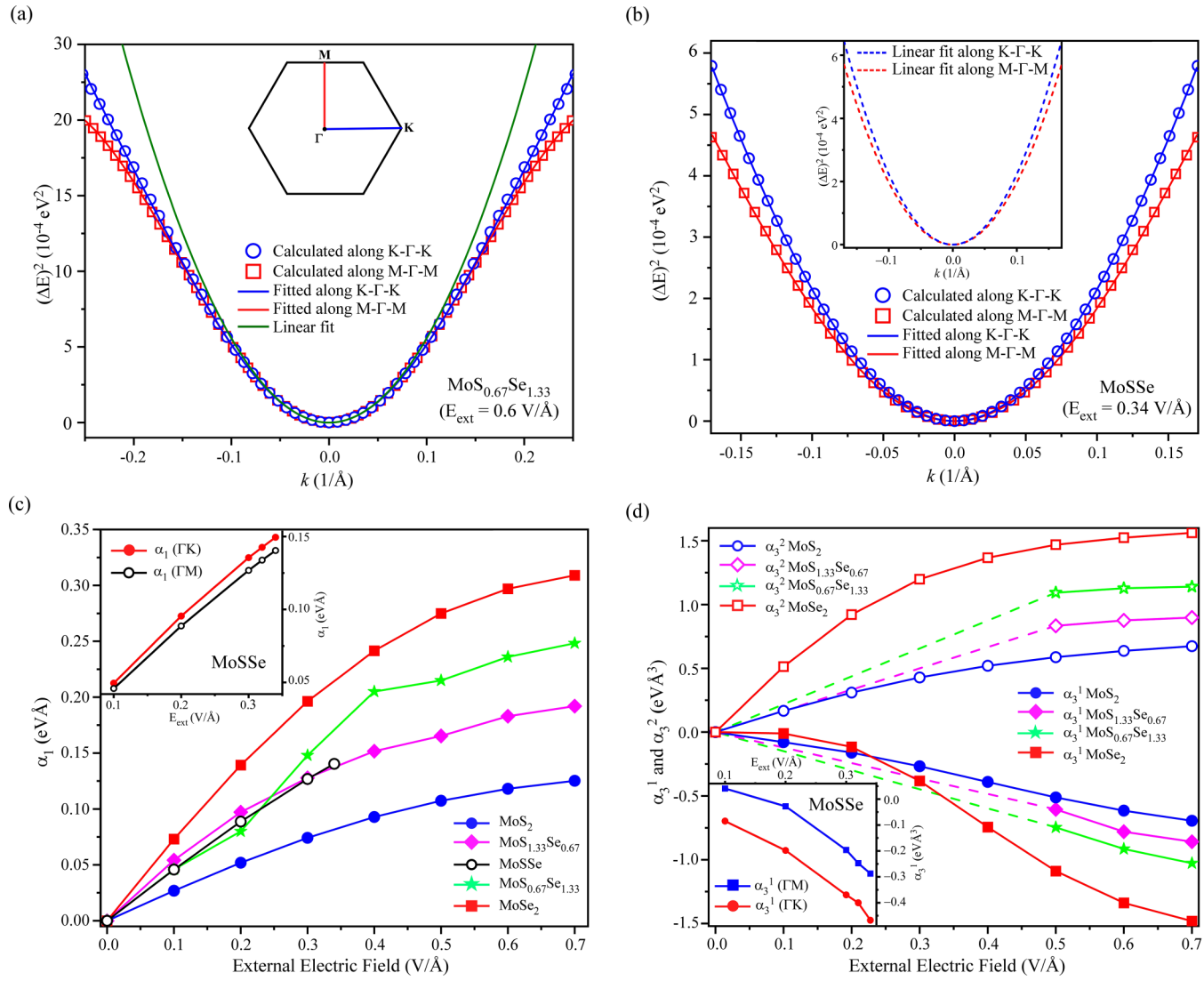

FIG. 4. The square of the Rashba splitting energy $\Delta E^2(k)$ for the valence bands for (a) $MoS_{0.67}Se_{1.33}$ at 0.6 V/Å and (b) MoSSe at ∼0.34 V/Å along the Γ-*M* (blue circles) and Γ-*K* (red squares) directions. The olive line shows the first-order fit, and the blue and red lines show the third-order fits. The blue and red dotted lines in the inset of (b) show the two independent first-order fits. The variation of the (c) first-order and (d) third-order terms of Rashba splitting in all alloys as a function of the external electric field. All Rashba terms for the MoSSe system are shown separately in the insets to highlight their anisotropy.

However, for the C_{2v} system, both A and B are θ dependent, and the values of $\Delta E(k)$ along Γ-$K(\theta = 0)$ and Γ-$M(\theta = \pi/2)$ are given as

$$[\Delta E(k, \theta = 0)]^2 = \left(\alpha_{R,x}k + \alpha_3^1\, k^3\right)^2, \tag{13}$$

$$[\Delta E(k, \theta = \pi/2)]^2 = \left(\alpha_{R,y}k + \alpha_3^4\, k^3\right)^2. \tag{14}$$

By fitting the two equations along the Γ-*M* and Γ-*K* directions of the MoSSe structure, we can obtain the values of the two linear parameters (by parabolic fitting as before) as well as the two third-order terms α_3^1 and α_3^4. The DFT-calculated results for the Rashba energy splitting in MoSSe at 0.34 V/Å after fitting them using Eqs. (13) and (14) are shown in Fig. 4(b). The values of the four parameters $\alpha_{R,x}$, $\alpha_{R,y}$, α_3^1, and α_3^4 come out to be ∼0.149 eVÅ, 0.140 eVÅ, −0.287 eVÅ^3, and −0.467 eVÅ^3, respectively, and the linear parameters are plotted separately in the inset of Fig. 4(b). Comparing Eqs. (13) and (14) with Eq. (7), it is obvious that α_3^1 and α_3^4 in the C_{2v} system play the role of α_3^1 in C_{3v} systems with no parameters in C_{2v} to replicate the role of $(\alpha_3^2)_{C_{3v}}$. This is evident from the fact that, when Eq. (7) is fitted to the Γ-*K* or Γ-*M* of MoSSe, the value of $(\alpha_3^2)_{C_{3v}}$ always comes out to be zero for all fields. However, α_3^1 and α_3^4 in C_{2v} are mutually independent and thus contribute to the Rashba anisotropy.

The linear and higher-order Rashba parameters for all the structures at different electric fields up to 0.7 V/Å are plotted in Figs. 4(c) and 4(d), respectively. Just like the nonrelativistic calculations, the DFT+SOC calculations also indicate that MoSSe becomes metallic around an electric field of ∼0.35 V/Å. The two linear terms $\alpha_{R,x}$ and $\alpha_{R,y}$ along the Γ-*K* and Γ-*M* directions in the MoSSe structure have been labeled as $\alpha_1(\Gamma K)$ and $\alpha_1(\Gamma M)$, respectively, for convenience. The $\alpha_1(\Gamma M)$ term of MoSSe is plotted with the α_1 terms of the other structures in Fig. 4(c), and both first-order terms have

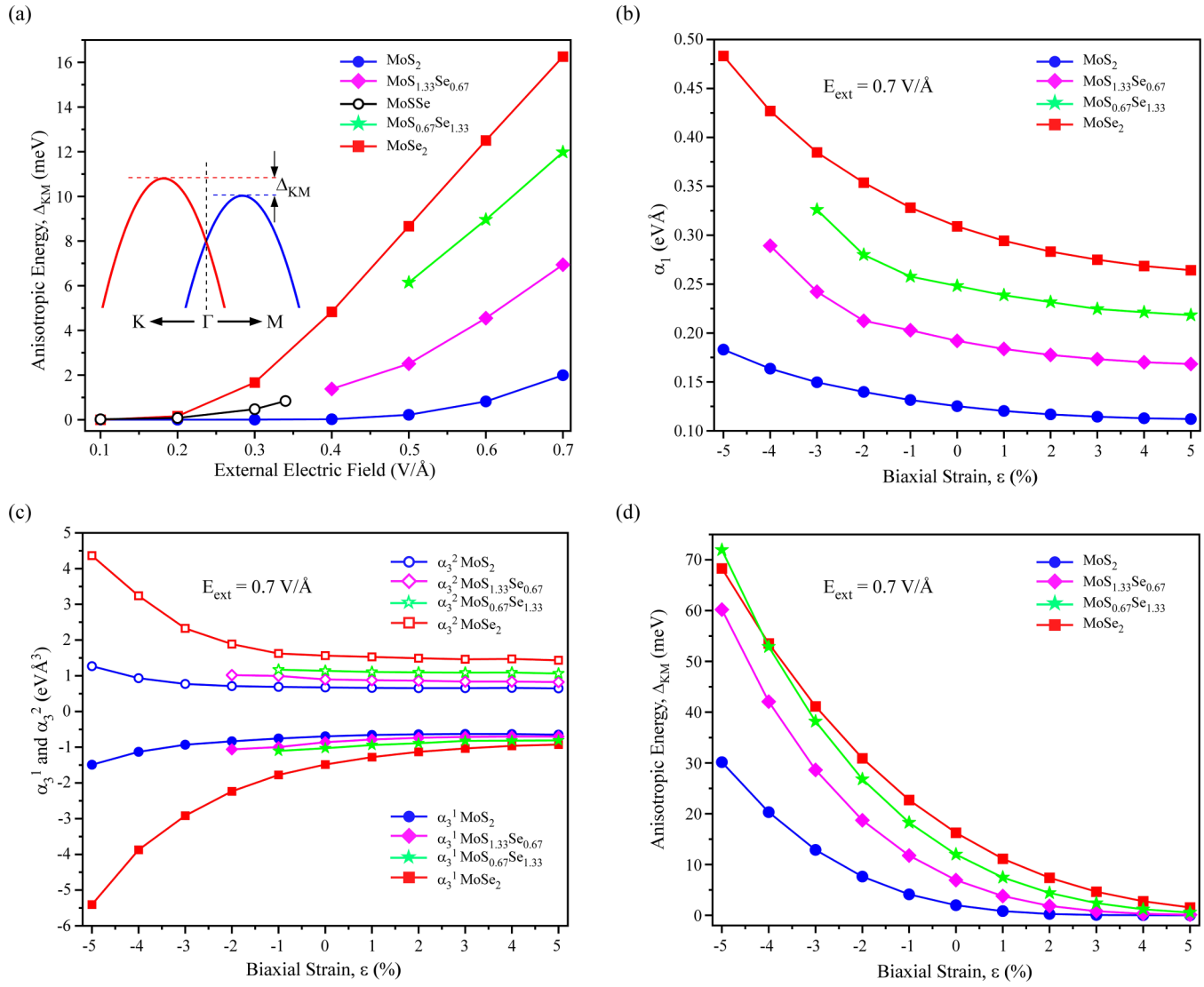

FIG. 5. (a) The anisotropic energies (Δ_{KM}) of all alloys plotted as a function of the external electric field. Variation of (b) first-order and (c) third-order terms in C_{3v} structures at an external electric field of 0.7 V/Å as a function of the biaxial strain. (d) Biaxial strain dependence of the anisotropic energies (Δ_{KM}) of C_{3v} structures at an external electric field of 0.7 V/Å.

been shown separately in the inset of Fig. 4(c) to compare them directly. All α_1 terms are very sensitive to the applied voltage and increase monotonically with the field. $MoSe_2$ shows the maximum increase in α_1 and has the highest value of the linear Rashba parameter at a given electric field. MoS_2, on the other hand, has the least α_1 value, with the other structures occupying intermediate positions based on their relative chalcogen content (x). The structures with greater percentage of the larger-sized Se atoms show higher values of the first-order coefficient than the other structures at higher electric field values. Thus, the order of magnitude of the α_1 values for high fields follow the trend $MoSe_2 > MoS_{0.67}Se_{1.33} > MoSSe > MoS_{1.33}Se_{0.67} > MoS_2$. This trend is somewhat disturbed at relatively lower fields due to the band hybridization appearing in the valence bands of the $MoS_{0.67}Se_{1.33}$ and $MoS_{1.33}Se_{0.67}$ structures. Although this type of hybridization prevents us from calculating the higher-order terms accurately, it has been shown to give rise to the unconventional Rashba effect [64]. All the other computable third-order terms for all the structures except MoSSe have been shown in Fig. 4(d). As MoSSe has two independent third-order parameters, they are shown separately in the inset of Fig. 4(d). The α_3^1 and α_3^2 values for the C_{3v} alloys are always negative and positive, respectively, and strongly depend on the strength of the applied voltage. The magnitudes of both parameters show a similar trend as the linear one, with $MoSe_2$ bagging the highest values and MoS_2 the least of all the structures. The remaining alloys have intermediate values based on their Se content. Thus, it is evident that the nature of the chalcogen atoms present and the system symmetry plays a significant role in deciding the magnitude and profile of the Rashba effect.

In terms of energy, the extent of anisotropy present in the system can be estimated from the anisotropic energy (Δ_{KM}), as discussed before. The anisotropic energy for the different alloy structures at different electric fields has been plotted in Fig. 5(a). For the C_{3v} systems, α_3^2 is primarily

responsible for the anisotropic energy splitting, and as expected, it leads to $MoSe_2$ having the greatest Δ_{KM} value. $MoS_{0.67}Se_{1.33}$, $MoS_{1.33}Se_{0.67}$, and MoS_2 have decreasing values of Δ_{KM}, with MoS_2 having the least of all the alloys. Unlike the C_{3v} systems, the C_{2v} MoSSe structure has no isotropic terms. All the first- and third-order terms are anisotropic and contribute to the anisotropic splitting. If the Δ_{KM} value for the MoSSe structure is extrapolated for the higher electric fields, it can be estimated to occupy the position intermediate between $MoS_{0.67}Se_{1.33}$ and $MoS_{1.33}Se_{0.67}$. However, the structure becomes metallic at a relatively low field. Thus, although the origin of anisotropy is different for different symmetry systems, the anisotropic splitting energy appears to depend on the nature of the chalcogen atoms in all the alloys.

In addition to tuning the band gaps of semiconductors, strain has been utilized to modify the Rashba effect in polar materials [65–68]. We have investigated the possibility of such manipulation in the linear part of the Rashba effect for nonpolar materials under an electric field. Additionally, we have also studied the effect of biaxial strain on the nonlinearity and anisotropy of the Rashba effect. The Rashba splittings for all the C_{3v} structures are calculated for different compressive and tensile biaxial strain values ranging from -5 to 5% in a constant electric field of $0.7\,V/Å$. The variations of the linear parameters, the nonlinear parameters, and the anisotropic energies (Δ_{KM}) with the biaxial strain are shown in Figs. 5(b)–5(d), respectively. The application of tensile strain tends to decrease the linear portion of the Rashba effect in the alloys, just as it does in the polar TMDs, as reported earlier [65]. Additionally, it also decreases the nonlinearity and the anisotropy present in the Rashba splittings. On the other hand, compressive strain significantly enhances the linear and third-order terms, increasing the magnitude, nonlinearity, and anisotropy of the Rashba effect. The hierarchy of the Rashba parameters in the different alloys is maintained under the application of strain, with $MoSe_2$ always having the maximum and MoS_2 the minimum values among all the structures. In terms of percentage, $MoSe_2$ shows an increase of $\sim$56% in the first-order Rashba parameter at -5%, whereas MoS_2 shows an increase of $\sim$46% for the same amount of strain (see Fig. S8 in the Supplemental Material [52]). At higher values of compressive strain, the valence bands of $MoS_{0.67}Se_{1.33}$ and $MoS_{1.33}Se_{0.67}$ undergo hybridizations and disturb the Rashba effect. As a result, the first-order term decreases after ~ -3% of strain (not shown), and the higher-order terms cannot be accurately calculated. Another consequence of the band hybridization is the increase in the anisotropic splitting energy, which causes Δ_{KM} of $MoS_{0.67}Se_{1.33}$ to exceed that of $MoSe_2$ at 5% compressive strain.

IV. CONCLUSIONS

To summarize, we have introduced the Rashba effect in the thermodynamically stable nonpolar TMD alloys by breaking the out-of-plane inversion symmetry using an external electric field. Using the CE method, we identify three stable $MoS_{2(1-x)}Se_{2x}$ alloys with different symmetries corresponding to $x = 0.33$, 0.5, and 0.67. Our results show that the direct band gaps of all the structures can be tuned using electric field and biaxial strain. While the tensile strain reduces the band gaps monotonically, applying compressive strain initially increases the gaps in these materials and then decreases them after ~ -2% strain. The species of the chalcogen atoms contributing to the valence bands plays a significant role in dictating the behavior of the band structures in the presence of strain. Under a perpendicular external electric field, the MoSSe alloy undergoes a semiconductor-to-metallic transition at a field of $\sim 0.35\,V/Å$, whereas all the other structures experience the transition at relatively higher electric fields, making MoSSe a suitable candidate for tunable optoelectronic devices. Unlike the linear and isotropic Rashba effect found in the polar TMD materials, these alloys exhibit nonlinear and anisotropic Rashba splittings, which require incorporating higher-order terms to accurately model their behavior. The magnitude of the linear and the higher-order terms in the Rashba Hamiltonian depends on the nature of the chalcogen atoms, and the alloys with a higher concentration of the larger-sized Se atoms have higher values of the Rashba parameters than others. While the large anisotropy in the MoS_2, $MoSe_2$, $MoS_{0.67}Se_{1.33}$, and $MoS_{1.33}Se_{0.67}$ structures primarily stems from a third-order anisotropic term (α_3^2), all the first- and third-order terms in MoSSe are anisotropic and contribute to the anisotropy in the system. The magnitude, nonlinearity, and anisotropy can all be increased significantly by increasing the applied field. Finally, we have also studied the effect of biaxial strain on the electric-field-generated Rashba parameters in the C_{3v} structures. We discover that, while all the parameters decrease gradually with an increase in the tensile strain, they can be increased considerably by applying compressive strain. Our findings introduce a range of promising thermodynamically stable TMD alloys with highly tunable band gaps and anisotropic Rashba effect that can outperform the well-established Janus TMDs in spintronic and electronic applications.

ACKNOWLEDGMENTS

S.C. acknowledges CSIR [File No. 09/921(0348)/2021-EMR-I], Government of India, for financial support. We thank Prof. P. K. Panigrahi for the computational facility supported by DST, India, through Grant No. DST/ICPS/QuST/Theme-1/2019/Q-95.

[1] A. Splendiani, L. Sun, Y. Zhang, T. Li, J. Kim, C. Y. Chim, G. Galli, and F. Wang, Nano Lett. **10**, 1271 (2010).

[2] K. F. Mak, C. Lee, J. Hone, J. Shan, and T. F. Heinz, Phys. Rev. Lett. **105**, 136805 (2010).

[3] S. W. Han, H. Kwon, S. K. Kim, S. Ryu, W. S. Yun, D. H. Kim, J. H. Hwang, J.-S. Kang, J. Baik, H. J. Shin *et al.*, Phys. Rev. B **84**, 045409 (2011).

[4] B. Radisavljevic, A. Radenovic, J. Brivio, V. Giacometti, and A. Kis, Nat. Nanotechnol. **6**, 147 (2011).

[5] W. Bao, X. Cai, D. Kim, K. Sridhara, and M. S. Fuhrer, Appl. Phys. Lett. **102**, 042104 (2013).

[6] H. Kwon, S. Garg, J. H. Park, Y. Jeong, S. Yu, S. M. Kim, P. Kung, and S. Im, Npj 2D Mater. Appl. **3**, 9 (2019).

[7] M. M. Ugeda, A. J. Bradley, S.- F. Shi, F. H. da Jornada, Y. Z. Zhang, D. Y. Qui, W. Ruan, S.- K. Mo, Z. Hussain, Z.- X. Shen *et al.*, Nat. Mater. **13**, 1091 (2014).

[8] A. Chernikov, T. C. Berkelbach, H. M. Hill, A. Rigosi, Y. Li, B. Aslan, D. R. Reichman, M. S. Hybertsen, and T. F. Heinz, Phys. Rev. Lett. **113**, 076802 (2014).

[9] W. Choi, N. Choudhary, G. H. Han, J. Park, D. Akinwande, and Y. H. Lee, Mater. Today **20**, 116 (2017).

[10] W. Xin-Ran, S. Yi, and Z. Rong, Chin. Phys. B **22**, 098505 (2013).

[11] R. Cheng, S. Jiang, Y. Chen, Y. Liu, N. Weiss, H. C. Cheng, H. Wu, Y. Huang, and X. Duan, Nat. Commun. **5**, 5143 (2014).

[12] A. Daus, S. Vaziri, V. Chen, Ç. Köroğlu, R. W. Grady, C. S. Bailey, H. R. Lee, K. Schauble, K. Brenner, and E. Pop, Nat. Electron. **4**, 495 (2021).

[13] D. Akinwande, N. Petrone, and J. Hone, Nat. Commun. **5**, 5678 (2014).

[14] T. Cao, G. Wang, W. Han, H. Ye, C. Zhu, J. Shi, Q. Niu, P. Tan, E. Wang, B. Liu *et al.*, Nat. Commun. **3**, 887 (2012).

[15] H. Zeng, J. Dai, W. Yao, D. Xiao, and X. Cui, Nat. Nanotechnol. **7**, 490 (2012).

[16] K. F. Mak, K. He, J. Shan, and T. F. Heinz, Nat. Nanotechnol. **7**, 494 (2012).

[17] Y. Liu, Y. Gao, S. Zhang, J. He, J. Yu, and Z. Liu, Nano Res. **12**, 2695 (2019).

[18] Y. A. Bychkov and É. I. Rashba, Pis'ma Zh. Eksp. Teor. Fiz **39**, 66 (1984) [JETP Lett. **39**, 78 (1984)].

[19] Y. C. Cheng, Z. Y. Zhu, M. Tahir, and U. Schwingenschlögl, Europhys. Lett. **102**, 57001 (2013).

[20] A. Y. Lu, H. Zhu, J. Xiao, C. P. Chuu, Y. Han, M. H. Chiu, C. C. Cheng, C. W. Yang, K. H. Wei, Y. Yang *et al.*, Nat. Nanotechnol. **12**, 744 (2017).

[21] J. C. R. Sánchez, L. Vila, G. Desfonds, S. Gambarelli, J. P. Attané, J. M. De Teresa, C. Magén, and A. Fert, Nat. Commun. **4**, 2944 (2013).

[22] M. Isasa, M. C. Martínez-Velarte, E. Villamor, C. Magén, L. Morellón, J. M. De Teresa, M. R. Ibarra, G. Vignale, E. V. Chulkov, E. E. Krasovskii *et al.*, Phys. Rev. B **93**, 014420 (2016).

[23] T. S. Ghiasi, A. A. Kaverzin, P. J. Blah, and B. J. Van Wees, Nano Lett. **19**, 5959 (2019).

[24] H. Yuan, M. S. Bahramy, K. Morimoto, S. Wu, K. Nomura, B.-J. Yang, H. Shimotani, R. Suzuki, M. Toh, C. Kloc *et al.*, Nat. Phys. **9**, 563 (2013).

[25] S. Wu, J. S. Ross, G. B. Liu, G. Aivazian, A. Jones, Z. Fei, W. Zhu, D. Xiao, W. Yao, D. Cobden *et al.*, Nat. Phys. **9**, 149 (2013).

[26] C. Cheng, J. T. Sun, X. R. Chen, H. X. Fu, and S. Meng, Nanoscale **8**, 17854 (2016).

[27] Y. A. Bychkov and E. I. Rashba, J. Phys. C: Solid State Phys. **17**, 6039 (1984).

[28] L. Petersen and P. Hedegård, Surf. Sci. **459**, 49 (2000).

[29] A. Johansson, J. Henk, and I. Mertig, Phys. Rev. B **93**, 195440 (2016).

[30] X. Cartoixà, L. W. Wang, D. Z. Y. Ting, and Y. C. Chang, Phys. Rev. B **73**, 205341 (2006).

[31] S. Vajna, E. Simon, A. Szilva, K. Palotas, B. Ujfalussy, and L. Szunyogh, Phys. Rev. B **85**, 075404 (2012).

[32] S. Chakraborty and S. Raj, Phys. Rev. B **107**, 035420 (2023).

[33] T. Oguchi and T. Shishidou, J. Phys.: Condens. Matter **21**, 092001 (2009).

[34] E. Simon, A. Szilva, B. Ujfalussy, B. Lazarovits, G. Zarand, and L. Szunyogh, Phys. Rev. B **81**, 235438 (2010).

[35] D. Wang, L. Liu, N. Basu, and H. L. Zhuang, Adv. Theor. Simul. **3**, 2000195 (2020).

[36] J. Kang, S. Tongay, J. Li, and J. Wu, J. Appl. Phys. **113**, 143703 (2013).

[37] S. Susarla, A. Kutana, J. A. Hachtel, V. Kochat, A. Apte, R. Vajtai, J. C. Idrobo, B. I. Yakobson, C. S. Tiwary, and P. M. Ajayan, Adv. Mater. **29**, 1702457 (2017).

[38] J.-S. Kim, R. Ahmad, T. Pandey, A. Rai, S. Feng, J. Yang, Z. Lin, M. Terrones, S. K. Banerjee, A. K. Singh *et al.*, 2D Mater. **5**, 015008 (2017).

[39] Y. C. Lin, R. Torsi, D. B. Geohegan, J. A. Robinson, and K. Xiao, Adv. Sci. **8**, 2004249 (2021).

[40] J. Mann, Q. Ma, P. M. Odenthal, M. Isarraraz, D. Le, E. Preciado, D. Barroso, K. Yamaguchi, G. von Son Palacio, A. Nguyen *et al.*, Adv. Mater. **26**, 1399 (2014).

[41] Q. Feng, N. Mao, J. Wu, H. Xu, C. Wang, J. Zhang, and L. Xie, ACS Nano **9**, 7450 (2015).

[42] Y. Gao, J. Liu, X. Zhang, and G. Lu, J. Phys. Chem. C **125**, 774 (2021).

[43] J. H. Yang and B. I. Yakobson, Chem. Mater. **30**, 1547 (2018).

[44] K. Yaji, Y. Ohtsubo, S. Hatta, H. Okuyama, K. Miyamoto, T. Okuda, A. Kimura, H. Namatame, M. Taniguchi, and T. Aruga, Nat. Commun. **1**, 17 (2010).

[45] J. Krempaský, H. Volfová, S. Muff, N. Pilet, G. Landolt, M. Radović, M. Shi, D. Kriegner, V. Holý, J. Braun *et al.*, Phys. Rev. B **94**, 205111 (2016).

[46] G. Kresse and J. Furthmüller, Phys. Rev. B **54**, 11169 (1996).

[47] J. P. Perdew, K. Burke, and M. Ernzerhof, Phys. Rev. Lett. **77**, 3865 (1996).

[48] P. E. Blöchl, Phys. Rev. B **50**, 17953 (1994).

[49] A. Van de Walle, M. Asta, and G. Ceder, Calphad **26**, 539 (2002).

[50] A. Togo and I. Tanaka, Scr. Mater. **108**, 1 (2015).

[51] U. Herath, P. Tavadze, X. He, E. Bousquet, S. Singh, F. Muñoz, and A. H. Romero, Comput. Phys. Commun. **251**, 107080 (2020).

[52] See Supplemental Material at http://link.aps.org/supplemental/10.1103/PhysRevB.108.165402 for details on phonon calculations and derivation of the Rashba energy splitting from the Rashba Hamiltonian in the MoSSe alloy.

[53] J. Nowotny, C. C. Sorrell, L. R. Sheppard, and T. Bak, Int. J. Hydrogen Energy **30**, 521 (2005).

[54] J. J. Loferski, J. Appl. Phys. **27**, 777 (1956).

[55] W. S. Yun, S. W. Han, S. C. Hong, I. G. Kim, and J. D. Lee, Phys. Rev. B **85**, 033305 (2012).

[56] C. V. Nguyen and N. N. Hieu, Chem. Phys. **468**, 9 (2016).

[57] P. Johari and V. B. Shenoy, ACS Nano **6**, 5449 (2012).

[58] E. Scalise, M. Houssa, G. Pourtois, V. Afanas'ev, and A. Stesmans, Nano Res. **5**, 43 (2012).

[59] R. K. Defo, S. Fang, S. N. Shirodkar, G. A. Tritsaris, A. Dimoulas, and E. Kaxiras, Phys. Rev. B **94**, 155310 (2016).

[60] Q. Liu, L. Li, Y. Li, Z. Gao, Z. Chen, and J. Lu, J. Phys. Chem. C **116**, 21556 (2012).

[61] A. Ramasubramaniam, D. Naveh, and E. Towe, Phys. Rev. B **84**, 205325 (2011).

[62] T. Chu, H. Ilatikhameneh, G. Klimeck, R. Rahman, and Z. Chen, Nano Lett. **15**, 8000 (2015).
[63] Z. Y. Zhu, Y. C. Cheng, and U. Schwingenschlögl, Phys. Rev. B **84**, 153402 (2011).
[64] R. Song, N. Hao, and P. Zhang, Phys. Rev. B **104**, 115433 (2021).
[65] A. Rezavand and N. Ghobadi, Physica E **132**, 114768 (2021).
[66] Q. F. Yao, J. Cai, W. Y. Tong, S. J. Gong, J. Q. Wang, X. Wan, C. G. Duan, and J. H. Chu, Phys. Rev. B **95**, 165401 (2017).
[67] S.-B. Yu, M. Zhou, D. Zhang, and K. Chang, Phys. Rev. B **104**, 075435 (2021).
[68] T. Hu, F. Jia, G. Zhao, J. Wu, A. Stroppa, and W. Ren, Phys. Rev. B **97**, 235404 (2018).